Supporting Information for Chemically-Localized Resonant Excitons in Silver-Pnictogen Halide Double-Perovskites

Raisa-Ioana Biega,[†] Marina R. Filip,[*,‡,¶,§] Linn Leppert,[*,‖,†] and Jeffrey B. Neaton[*,¶,§,⊥]

†*Institute of Physics, University of Bayreuth, Bayreuth 95440, Germany*

‡*Department of Physics, University of Oxford, Clarendon Laboratory, Oxford, OX1 3PU, United Kingdom*

¶*Department of Physics, University of California, Berkeley, CA 94720, USA*

§*Materials Science Division, Lawrence Berkeley National Laboratory, Berkeley, CA 94720, USA*

‖*MESA+ Institute for Nanotechnology, University of Twente, 7500 AE Enschede, The Netherlands*

⊥*Kavli Energy NanoSciences Institute at Berkeley, Berkeley, CA 94720, USA*

E-mail: marina.filip@physics.ox.ac.uk; l.leppert@utwente.nl; jbneaton@lbl.gov

Methodological Details

GW approximation

We obtain quasiparticle (QP) energies, and thus fundamental band gaps and band structures, by using Green's function-based many-body perturbation theory (MBPT),[1,2] a formalism that has been used with great success for solids,[3–5] interfaces,[6] and molecules.[7] In standard MBPT calculations, the QP eigensystem is most commonly obtained by solving one-particle equations

$$[-\frac{1}{2}\nabla^2 + V_{ext} + V_H + \Sigma(E^{QP}_{n\boldsymbol{k}})]\psi^{QP}_{n\boldsymbol{k}} = E^{QP}_{n\boldsymbol{k}}\psi^{QP}_{n\boldsymbol{k}}, \tag{S1}$$

in which $\Sigma = iG_0W_0$ is the non-local, energy-dependent self-energy operator. G_0 and W_0 are the zeroth-order one-particle Green's function and screened Coulomb interaction, respectively, here constructed from a DFT eigensystem calculated using the local density approximation (LDA). $E^{QP}_{n\boldsymbol{k}}$ and $\psi^{QP}_{n\boldsymbol{k}}$ are the QP energies and wavefunctions, respectively. Assuming that $\psi^{QP}_{n\boldsymbol{k}} = \psi^{LDA}_{n\boldsymbol{k}}$, Eq. S1 can be solved approximately at the level of first-order perturbation theory, namely

$$E^{\mathrm{QP}}_{nk} = E^{\mathrm{LDA}}_{nk} + Z(E^{\mathrm{LDA}}_{nk})\langle\psi_{nk}|\Sigma(E^{\mathrm{LDA}}_{nk}) - V_{xc}|\psi_{nk}\rangle, \tag{S2}$$

where V_{xc} is the LDA exchange-correlation potential, and $Z(E^{\mathrm{LDA}}_{nk}) = \left[1 - \frac{\partial\,\mathrm{Re}(\Sigma)}{\partial\omega}\big|_{\omega=E^{\mathrm{LDA}}_{nk}}\right]^{-1}$ is the QP renormalization factor.

Bethe-Salpeter equation

We calculate optical excitations by solving the Bethe-Salpeter equation (BSE)[8–11] with the Tamm-Dancoff approximation (TDA)[11] for each exciton state S. In reciprocal space, this equation takes the form

$$(E^{QP}_{c\boldsymbol{k}} - E^{QP}_{v\boldsymbol{k}})A^S_{vc\boldsymbol{k}} + \sum_{v'c'\boldsymbol{k'}} \langle vc\boldsymbol{k}|\, K^{eh}\, |v'c'\boldsymbol{k'}\rangle = \Omega^S A^S_{vc\boldsymbol{k}}, \tag{S3}$$

where $A^S_{vc\boldsymbol{k}}$ are the coefficients of the exciton wave function written in the free electron and hole basis $|vc\boldsymbol{k}\rangle$, Ω^S is the excitation energy, and K^{eh} is the electron-hole interaction kernel.[9] The optical absorption spectrum can be obtained from the imaginary part of the transverse dielectric function:

$$\varepsilon_2(\omega) = \frac{16\pi^2 e^2}{\omega^2} \sum_S \left| \hat{e} \cdot \sum_{vc\boldsymbol{k}} A^S_{vc\boldsymbol{k}} \langle v\boldsymbol{k}| \hat{p} |c\boldsymbol{k}\rangle \right|^2 \delta(\omega - \Omega^S), \tag{S4}$$

where $\hat{p}$ is the momentum operator and $\hat{e}$ is the direction of polarization of light.

In order to quantify the spatial extent of the exciton, we employ a similar approach as in Ref. 12 and define the electron–hole correlation function $F_S(\mathbf{r}) = \int_\Omega d^3\mathbf{r}_h |\Psi_S(\mathbf{r}_e = \mathbf{r}_h + \mathbf{r}, \mathbf{r}_h)|^2$. $F_S(\mathbf{r})$ provides the probability of finding electron and hole pair separated by the vector $\mathbf{r} = \mathbf{r_e} - \mathbf{r_h}$. We compute the integral as a discrete sum over $\mathbf{r}_h$, with $\mathbf{r}_h$=$\mathbf{r}(\mathrm{Ag}^+)$, $\mathbf{r}(\mathrm{B}^{3+})$ and $\mathbf{r}(\mathrm{X}^-)$. To approximately account for the symmetry and finite number of hole positions, we introduce the weight w_h and normalize $F_S(\mathbf{r})$ with respect to its cumulative sum:

$$F_S(\mathbf{r}) = \frac{\sum_h \left(|\Psi_S(\mathbf{r}_e = \mathbf{r}_h + \mathbf{r}, \mathbf{r}_h)|^2 \cdot w_h\right)}{\sum_{e,h} \left(|\Psi_S(\mathbf{r}_e, \mathbf{r}_h)|^2 \cdot w_h\right)} \tag{S5}$$

where $w_h = \begin{cases} 6 & \text{for } \mathbf{r}_e = \mathbf{r}(\mathrm{X}^-) \\ 1 & \text{otherwise} \end{cases}$. Using the distribution function defined in expression S5, we compute the average electron-hole separation $\sigma_{\mathbf{r}} = \sqrt{\langle |\mathbf{r}|^2 \rangle - \langle |\mathbf{r}| \rangle^2}$, where $\langle |\mathbf{r}|^n \rangle = \int_\Omega d^3\mathbf{r} |\mathbf{r}|^n F_S(\mathbf{r})$, and use it to quantify the degree of localization of the excitonic wave function.

Computational Details

Electronic structure

We calculate the DFT band structure of $Cs_2AgBiBr_6$ within the LDA[13,14] using the Quantum espresso software package.[15,16] We use a set of norm-conserving, fully relativistic Troullier-Martins[17] pseudopotentials, as previouslly reported in Ref. 18, with the following atomic configurations: $5s^25p^66s^1$ for Cs, $4s^24p^64d^{10}5s^1$ for Ag, $5d^{10}6s^26p^3$ for Bi, $4d^{10}5s^25p^3$ for Sb, $4s^24p^5$ for Br and $3s^23p^5$ for Cl.

For the ground-state calculations, the Kohn-Sham orbitals are expanded in plane-wave basis sets with a cutoff energy of 150 Ry and the Brillouin zone is sampled using an unshifted $10 \times 10 \times 10$ uniform k-point mesh, comprising 220 irreducible points. The LDA eigensystem is then used to construct the zeroth-order one-particle Green's function G_0 and screened Coulomb interaction W_0 in order to obtain the QP band structure. We include fully-relativistic spin-orbit coupling (SOC) in the construction of G_0 and W_0 for all materials. For these calculations, we use the BerkeleyGW software package,[19] with the generalized plasmon-pole method of Godby and Needs.[20] We use a total of 600 bands, a polarizability cutoff of 10 Ry and an energy cutoff of 60 Ry for the bare Coulomb interaction. With these settings our QP band gaps are converged to within 50 meV. DFT-LDA and G_0W_0@LDA band structures are obtained by Wannier interpolation using the Wannier90 code[21] and are shown in Figure S1 for all materials. We construct a set of maximally localized Wannier functions for the interpolation of the DFT band structure of Cs_2AgBX_6 in the vicinity of the band gap using the Ag-s, Ag-d, B-s, B-p and X-p states as the initial guess, leading to 42 and 24 maximally localized Wannier functions for the valence and conduction bands, respectively. To obtain accurate effective masses (reported in Table S1), it is important that both valence and conduction states are interpolated over simultaneously.

Calculation of effective masses

In order to compute the effective mass tensor, we calculate the second derivatives of the valence and conduction band edges with respect to the wave vector $\boldsymbol{k}$ along the three crystallographic directions

$$\frac{1}{m^*_{\alpha\beta}} = \frac{1}{\hbar^2}\frac{\partial^2 \varepsilon}{\partial k_\alpha \partial k_\beta} \tag{S6}$$

for $\alpha, \beta = x, y, z$. We calculate the second-order partial derivatives using finite differences in the first order. The effective mass tensor is diagonalized for the conduction and valence band to obtain the electron and hole effective masses, respectively. We calculate the isotropic hole and electron effective masses as the harmonic mean $m^* = \dfrac{3m_1m_2m_3}{m_1m_2 + m_2m_3 + m_3m_1}$ of the valence and conduction band effective masses, respectively, where the indices correspond to three orthogonal directions in a reference frame where the matrix of partial derivatives is diagonal. The effective mass m_3 corresponds to the direction from X to Γ (longitudinal), while m_1 and m_2, the transverse effective masses, correspond to the two directions perpendicular to that path.

In Table S1 we report the effective masses of Cs_2AgBX_6 (B=Bi, Sb and X=Br, Cl) at the point of the lowest direct transition calculated with DFT-LDA and G_0W_0@LDA, respectively. Note, that the CBM at X is almost dispersionless. We therefore approximate the reduced effective mass with the isotropic hole effective mass: $\dfrac{1}{\mu} = \dfrac{1}{m^*_h}$. In contrast, for $Cs_2AgSbBr_6$ the lowest direct transition is at L instead of at X. We find that at L the VBM changes its curvature along two of the three orthogonal directions, leading to an ill-defined hole effective mass. We therefore approximate the reduced effective mass of $Cs_2AgSbBr_6$ with the isotropic electron effective mass: $\dfrac{1}{\mu} = \dfrac{1}{m^*_e}$.

We compute the effective masses by evaluating the second derivative of the electronic band energy numerically on a dense reciprocal space grid. In Table S2 we show that the grid spacing introduces an uncertainty of up to ∼14% in the hole effective mass. Furthermore, the interpolation scheme (linear vs Wannier) used to compute the energies of the bands

introduces a systematic error of ∼8%. We also observe a subtle dependence of the effective masses on the DFT starting point (also shown in Table S2). Using the linear interpolation scheme, the hole effective masses calculated with G_0W_0@LDA and G_0W_0@PBE are the same. However, the electron effective mass is ill-defined using G_0W_0@PBE. Wannier interpolation leads to a difference of ∼10% (20%) between the G_0W_0@LDA and G_0W_0@PBE hole (electron) effective masses. All effective masses reported in the main text were calculated using the Wannier interpolation scheme within the G_0W_0@LDA approximation and using a grid spacing of $0.02\,\text{Å}^{-1}$.

We quantify the anisotropy of the effective mass tensor by introducing the anisotropy factor λ as defined in Ref. 22:

$$\lambda = \left(\frac{m_\perp}{m_\parallel}\right)^{1/3}, \tag{S7}$$

where $m_\perp = \dfrac{2m_{h_1}m_{h_2}}{m_{h_1}+m_{h_2}}$ is the harmonic mean of the transverse effective masses and $m_\parallel = m_{h_3}$ is the longitudinal hole effective mass. The limit $\lambda \to 1$ defines the case of a fully isotropic effective mass, while $\lambda > 1$ reflects the fact that the longitudinal effective mass is smaller than the transverse one. In table S1 we show that the hole effective mass is highly anisotropic, with the longitudinal component at least 4 times smaller than the transverse components. The valence band along X to Γ is very disperse, leading to a light longitudinal hole effective mass. Qualitatively, we find that the larger the anisotropy of the hole effective mass, the larger the deviation between the first principles exciton binding energy as compared to the Wannier-Mott model. This observation does not hold for $Cs_2AgSbBr_6$, for which the lowest direct transition is at L and the Wannier-Mott exciton binding energy is dominated by the almost completely isotropic electron effective mass.

Following the approach described by Schindlmayr in Ref. 22, we rewrite the Wannier-Mott binding energy taking into account the effect of effective mass anisotropy and define

the corrected exciton binding energy as

$$E_x(\lambda) = -3\left(\frac{1}{\varepsilon_\infty}\right)^2\left(\frac{2}{m_\perp}+\frac{1}{\lambda^2 m_\parallel}\right)^{-1}\left(\frac{\operatorname{arcsinh}\sqrt{\lambda^2-1}}{\sqrt{\lambda^2-1}}\right)^2 R_H. \tag{S8}$$

In Table S3 we show that by including the effective mass anisotropy in the Wannier-Mott model, the difference between the Wannier-Mott exciton binding energies and our first principles results decreases. The correction to the isotropic Wannier-Mott model increases with increasing anisotropy factor. We attribute the remaining difference between the BSE and Wannier-Mott exciton binding energies to an interplay of local field effects and the non-parabolicity of the band edges.

Optical properties

In our solution of the BSE, we use the Tamm-Dancoff approximation (TDA)[11] for the electron-hole interaction kernel K_{eh}. K_{eh} is expanded in a set of 22 valence and 22 conduction bands, and interpolated from a $4\times4\times4$ coarse k-point grid to a fine grid of $12\times12\times12$ points. The solution of the BSE is then computed using 16 occupied and 8 unoccupied states. In Figure S2 we show that, with these settings, the exciton binding energy of the first two excited states is converged to within better than 10 meV.

To address the significant difference between our computed exciton binding energy of 170 meV and the one reported in Ref. 23 (340 meV), we performed extensive tests. In particular, we tested the effect of using the generalized gradient approximation of Perdew-Burke-Ernzerhof[24] (PBE) as exchange-correlation (xc) functional in our DFT calculations. We show in Table S4 that the DFT starting point does not affect the value of the indirect band gap of $Cs_2AgBiBr_6$, but slightly changes the direct gap. Moreover, the use of PBE red-shifts the excitonic peak by ∼50 meV and significantly increases the exciton binding energy by approximately 42% (see Figure S3). Additionally, we also computed the BSE optical absorption spectrum using the same $4\times4\times4$ k-point grid as employed in Ref.

23, and obtained an exciton binding energy of 301 meV for the first bright state. The remaining difference of ∼40 meV can be attributed to the use of a geometry-optimized crystal structure and partially self-consistent *GW* in Ref. 23. The latter opens the QP band gaps by ∼0.3 eV for $Cs_2AgBiBr_6$, likely also affecting the static dielectric constant. Furthermore, the experimental lattice parameter of the cubic $Fm\bar{3}m$ phase used in the present work differs by 0.05 Å from the optimized lattice parameter used by Palummo et al.[23]

We calculate the average electron-hole separation of the excitonic wave function, by computing the excitonic wave function on an $8 \times 8 \times 8$ supercell, a sufficiently large real-space supercell to accommodate the excitonic wave function and to ensure convergence. For $Cs_2AgBiBr_6$, we evaluate the sum in Eq. S5 by averaging over three different hole positions (hole fixed on a Bi ion site, hole fixed on a Ag ion site and hole fixed on a Br ion site) and over all three degenerate bright transitions that the lowest bright excitonic peak consists of, obtaining an average electron-hole separation of 6.6 Å. This value is similar to the average electron-hole separation of 6.3 Å obtained by averaging over the first bright transition and the Ag and Bi site only. In Figure 4b of the main text, we therefore report the average electron-hole separation using this averaging procedure. To visualize the excitonic wave function, we need to fix the position of the hole. For $Cs_2AgSbBr_6$, $\Psi_S(\mathbf{r}_e, \mathbf{r}_h = \mathbf{r}(Sb^{3+})) \simeq \Psi_S(\mathbf{r}_e, \mathbf{r}_h = \mathbf{r}(Ag^{+}))$, so we sum over these two hole positions and plot in Figure S7 the resulting excitonic wave function. For all the other systems, $\Psi_S(\mathbf{r}_e, \mathbf{r}_h = \mathbf{r}(B^{3+})) \gg \Psi_S(\mathbf{r}_e, \mathbf{r}_h = \mathbf{r}(Ag^{+}))$, and we plot only the excitonic wave function when the hole is fixed on a B ion site.

Table S1: Hole effective masses of $Cs_2AgBiBr_6$, $Cs_2AgBiCl_6$, $Cs_2AgSbCl_6$ and electron effective mass of $Cs_2AgSbBr_6$ at the band edges corresponding to the lowest direct transition (in units of the electron rest mass m_0, expressed in a reference frame where the effective mass tensor is diagonal) and the anisotropy factor λ, as computed with DFT-LDA and G_0W_0@LDA

		$\mathbf{m}_{h_1}$	$\mathbf{m}_{h_2}$	$\mathbf{m}_{h_3}$	$\mathbf{m}_h^*$	λ
LDA	$Cs_2AgBiBr_6$	0.79	0.73	0.17	0.36	1.65
G_0W_0		0.72	0.67	0.15	0.31	1.67
LDA	$Cs_2AgBiCl_6$	1.08	0.78	0.19	0.39	1.68
G_0W_0		0.75	0.56	0.17	0.33	1.57
LDA	$Cs_2AgSbCl_6$	1.25	0.98	0.17	0.39	1.86
G_0W_0		0.96	0.71	0.15	0.32	1.77
		$\mathbf{m}_{e_1}$	$\mathbf{m}_{e_2}$	$\mathbf{m}_{e_3}$	$\mathbf{m}_e^*$	
LDA	$Cs_2AgSbBr_6$	0.31	0.29	0.25	0.28	1.06
G_0W_0		0.33	0.30	0.26	0.29	1.07

Table S2: Effective masses and reduced mass at X (in units of the electron rest mass m_0), BSE and Wannier-Mott exciton binding energies (in meV) of cubic $Cs_2AgBiBr_6$ for LDA and PBE starting points

G_0W_0@LDA

Methodology (interpolation)	Grid spacing (1/Å)	Effective masses (m_0)			Binding energy (meV)			
		m_h^*	m_e^*	μ	E_x^{WM} w/ μ	E_x^{WM} w/ m_h^*	E_x^{BSE} $\epsilon(\mathbf{r},\mathbf{r}';\omega)$	E_x^{BSE} $\epsilon(\mathbf{r},\mathbf{r}';\omega)\to\varepsilon_\infty$
linear	0.093	0.325	1.229	0.257	100	126	170	99
Wannier	0.093	0.352	1.115	0.267	104	137		
	0.020	0.309	0.857	0.227	88	120		

G_0W_0@PBE

Methodology (interpolation)	Grid spacing (1/Å)	Effective masses (m_0)			Binding energy (meV)			
		m_h^*	m_e^*	μ	E_x^{WM} w/ μ	E_x^{WM} w/ m_h^*	E_x^{BSE} $\epsilon(\mathbf{r},\mathbf{r}';\omega)$	E_x^{BSE} $\epsilon(\mathbf{r},\mathbf{r}';\omega)\to\varepsilon_\infty$
linear	0.093	0.326	–	–	–	156	242	144
Wannier	0.093	0.317	0.878	0.233	111	151		
	0.020	0.269	0.652	0.191	91	128		

Table S3: Exciton binding energy (in meV) as computed within the G_0W_0+BSE approach ($\mathbf{E}_x^{BSE}$) and with the Wannier-Mott model ($\mathbf{E}_x^{WM}$). $\mathbf{E}_x(\lambda)$ is the exciton binding energy including effective mass anisotropy.

System	$\mathbf{E}_x^{BSE}$ (meV)	$\mathbf{E}_x^{WM}$ (meV)	$\mathbf{E}_x(\lambda)$ (meV)
$Cs_2AgBiBr_6$	170	120	148
$Cs_2AgBiCl_6$	333	205	240
$Cs_2AgSbBr_6$	247	112	113
$Cs_2AgSbCl_6$	434	193	250

Table S4: Comparison between the computational setup used in Ref. 23 and in the current work

Theory level	Input parameter	Palummo et al.[23]	Present work	
	lattice parameter	7.99 Å	7.94 Å	
DFT	xc functional	PBE	LDA	PBE
	cutoff energy	520 eV	2040 eV	680 eV
	k-point grid	8 x 8 x 8	$10 \times 10 \times 10$	$10 \times 10 \times 10$
GW	flavor	self-consistent *GW*	one-shot G_0W_0	one-shot G_0W_0
	cutoff energy for ε	40 eV	136 eV	54 eV
	cutoff energy for Σ_c	163 eV	136 eV	54 eV
	cutoff energy for Σ_x	1088 eV	816 eV	680 eV
	energy above VBM	∼40 eV	∼46 eV	∼46 eV
BSE	TDA	yes	yes	yes
	number of states in kernel	10 occupied 10 unoccupied	22 occupied 22 unoccupied	22 occupied 22 occupied
	input k-point grid	$4 \times 4 \times 4$	$4 \times 4 \times 4$	$4 \times 4 \times 4$
	interpolation k-point grid	—	$12 \times 12 \times 12$	$12 \times 12 \times 12$
	number of states on the interpolated k-point grid	—	16 occupied 8 unoccupied	16 occupied 8 unoccupied

Table S5: Comparison between *GW* band gaps and computed exciton binding energy obtained using *evGW* in Ref. 23 and using G_0W_0 in the current work

	xc functional	GW band gaps (eV)		Binding energy (meV)	
		$X^{VBM} \rightarrow L^{CBM}$	$X^{VBM} \rightarrow X^{CBM}$	dark	bright
evGW[23]	PBE	2.1	2.7	480	340
G_0W_0	PBE	1.66	2.34	346	242
	LDA	1.66	2.40	253	170

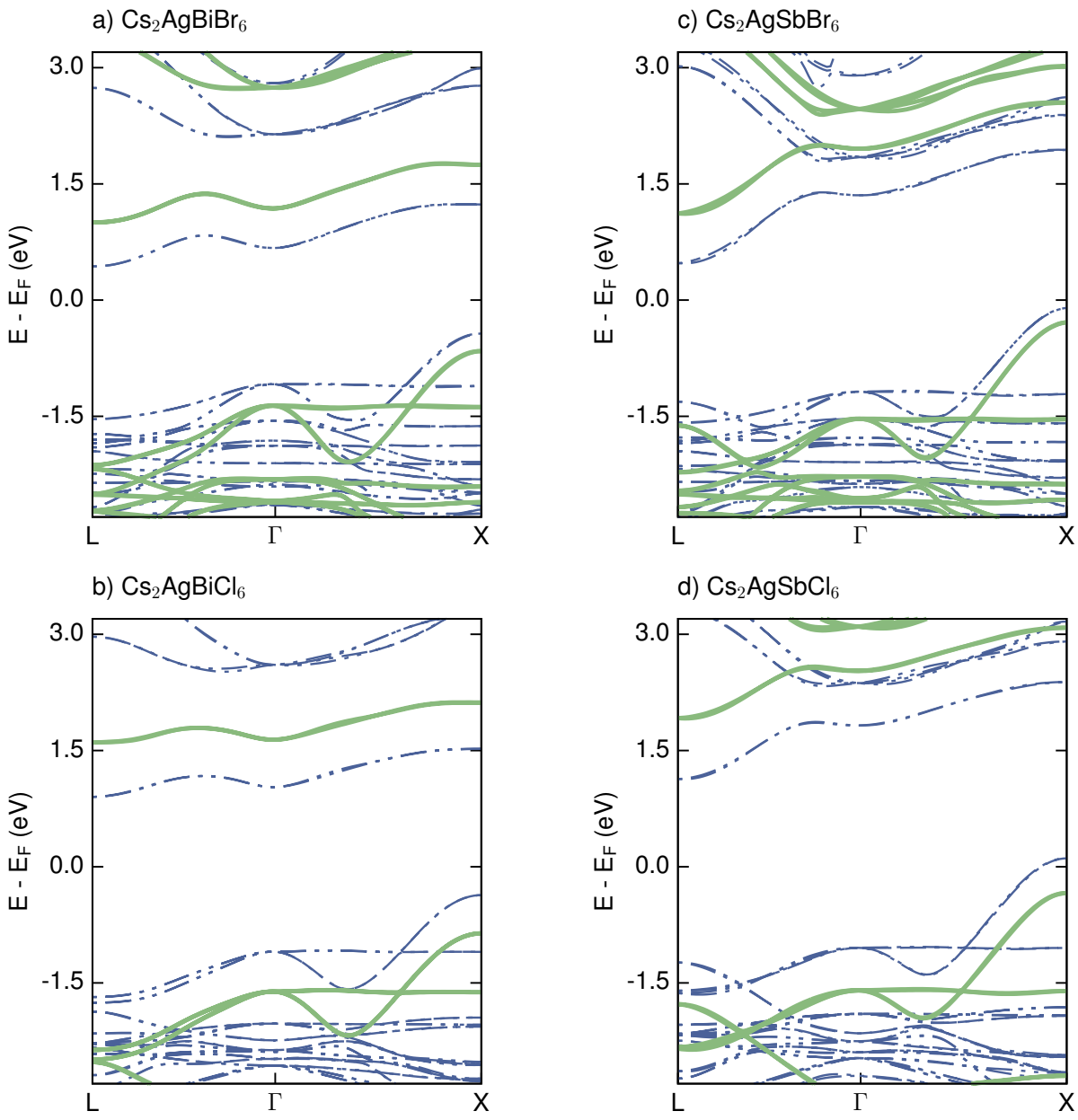

Figure S1: DFT-LDA (blue dashed line) and G_0W_0@LDA (green solid line) Wannierized band structures of a) $Cs_2AgBiBr_6$; b) $Cs_2AgBiCl_6$; c) $Cs_2AgSbBr_6$ and d) $Cs_2AgSbCl_6$

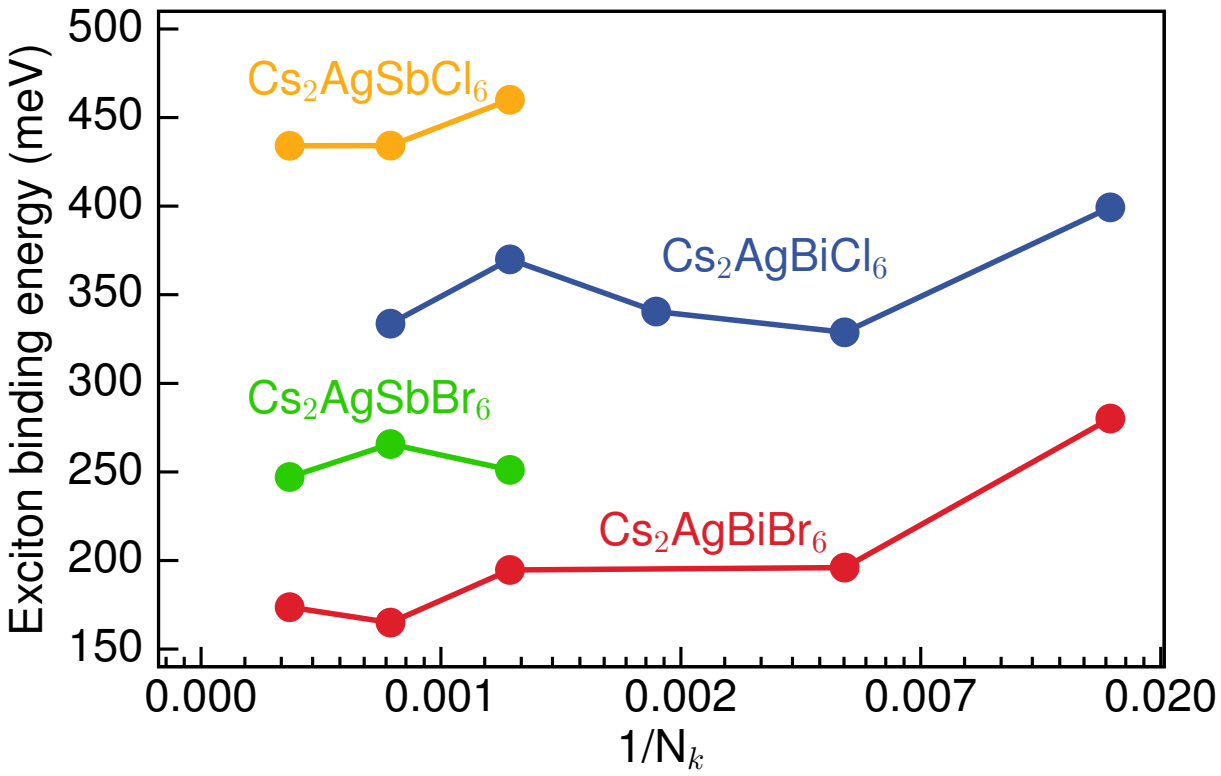

Figure S2: Convergence of the exciton binding energy with respect to the number of kpoints used for the interpolation of the kernel.

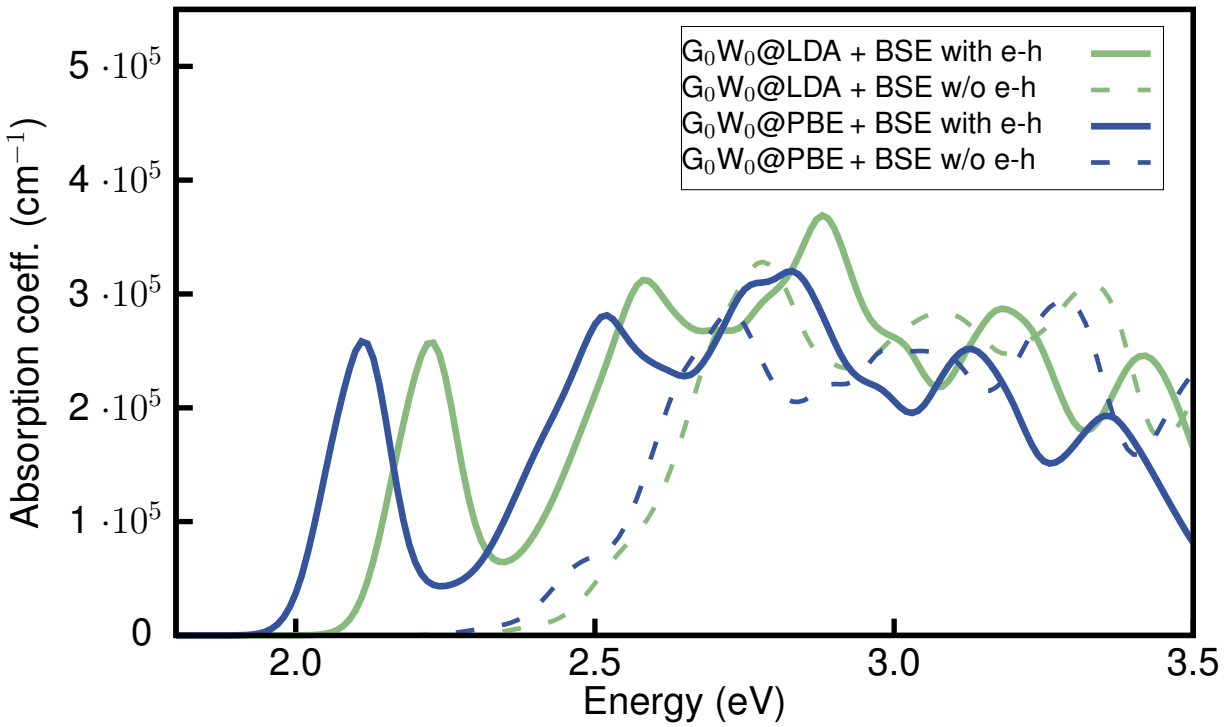

Figure S3: Optical absorption spectrum of $Cs_2AgBiBr_6$, where the independent particle spectrum is represented with dashed line and the BSE spectrum with green solid line. The results using DFT-LDA starting point are represented in green and the ones using DFT-PBE as starting point in blue.

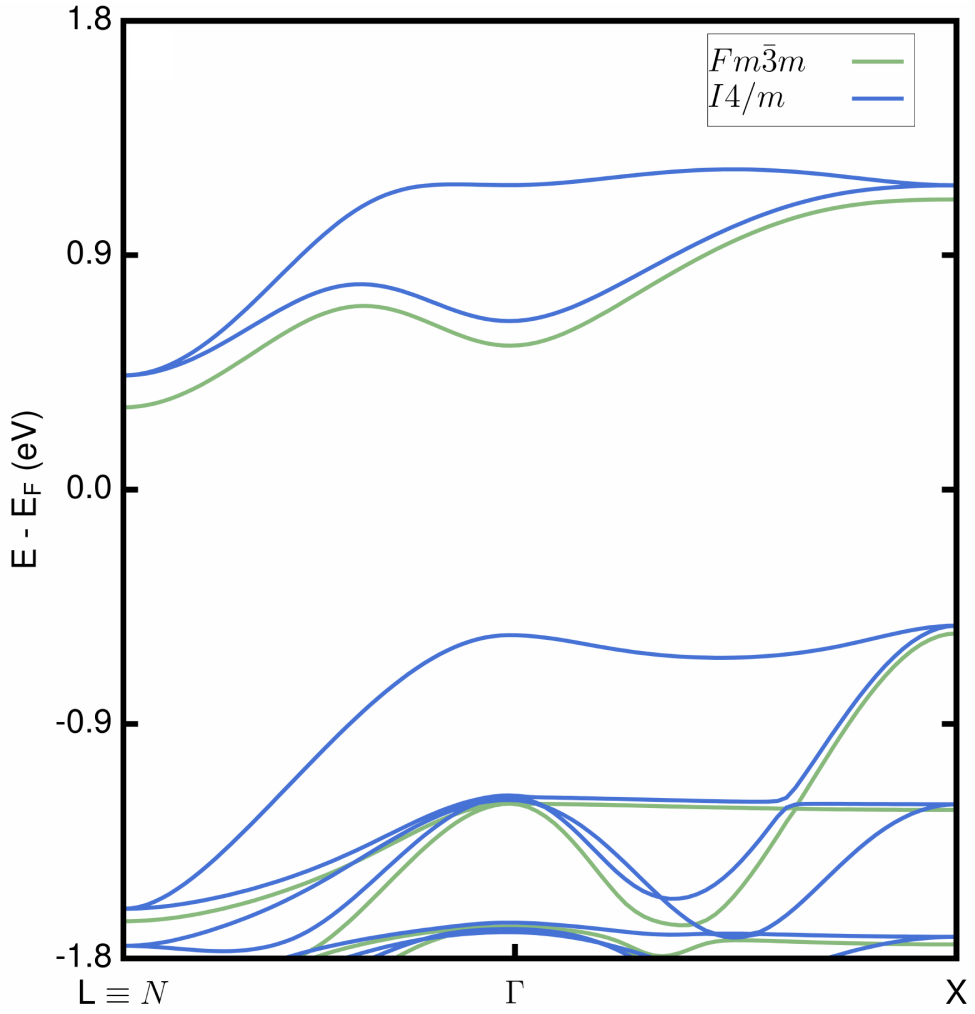

Figure S4: a) DFT-LDA band structure of $Cs_2AgBiBr_6$. The band structure of the primitive unit cell of the cubic $Fm\bar{3}m$ phase is represented in green and for the conventional unit cell of the tetragonal $I4/m$ phase in blue.

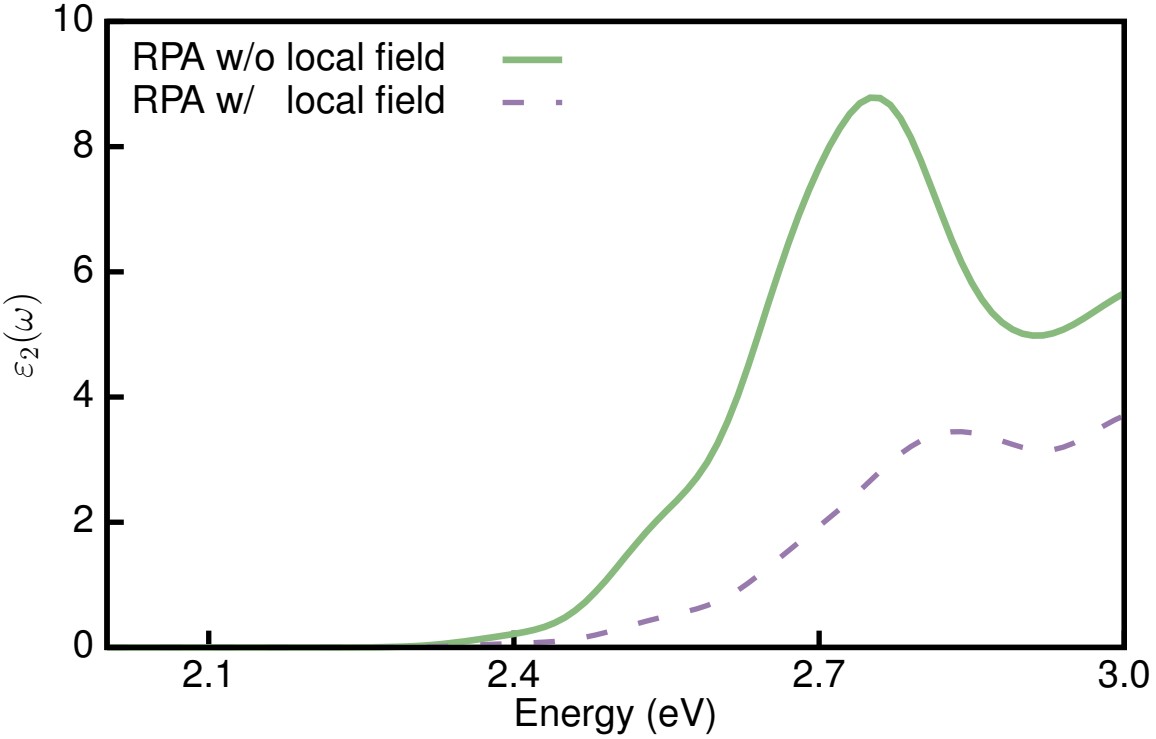

Figure S5: Imaginary part of the dielectric function as calculated within the random phase approximation with and without local field effects.

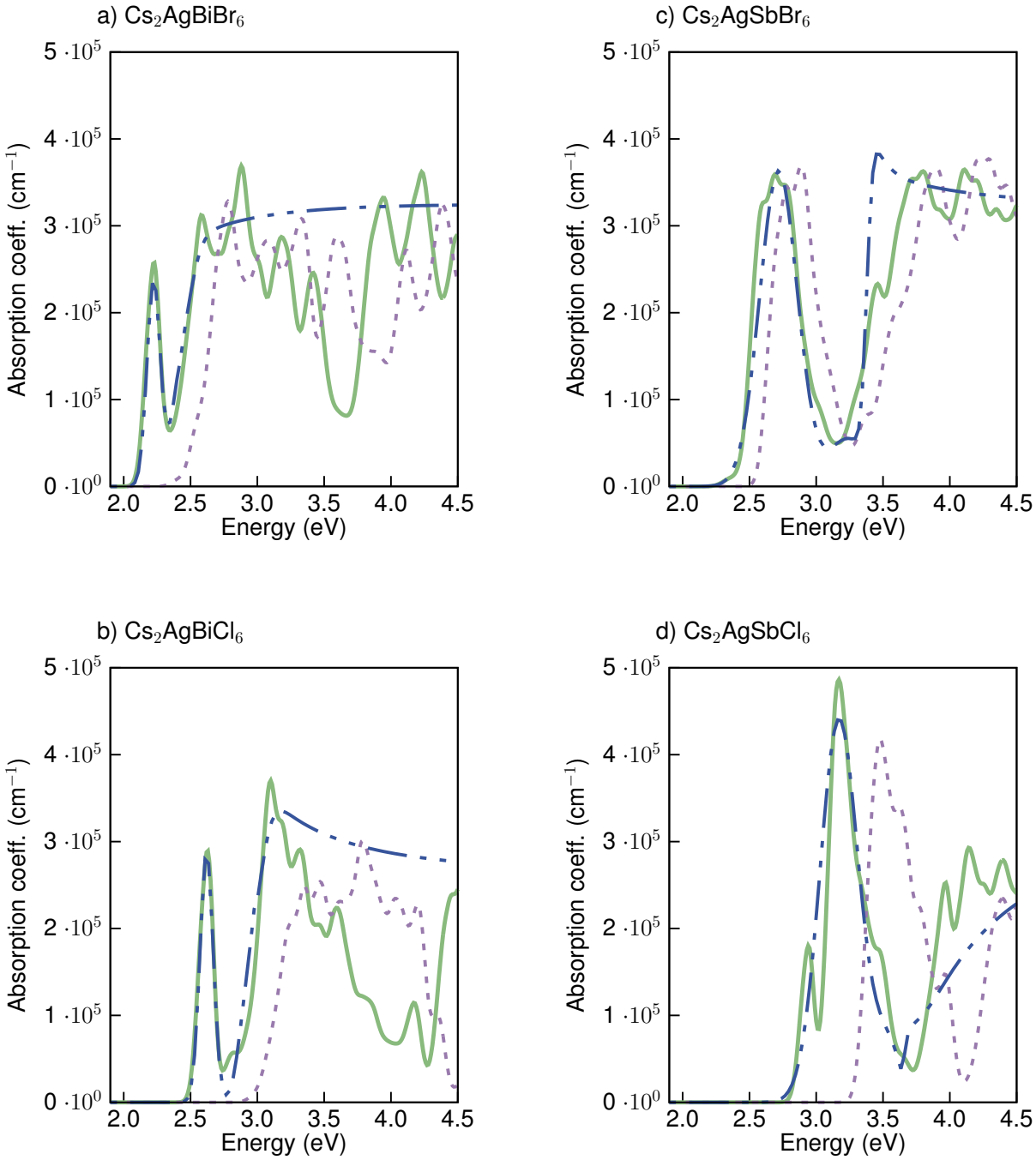

Figure S6: Optical absorption spectrum of a) $Cs_2AgBiBr_6$; b) $Cs_2AgBiCl_6$; c) $Cs_2AgSbBr_6$ and d) $Cs_2AgSbCl_6$, where the independent particle spectrum is represented with purple dashed line, the BSE spectrum with green solid line and the Elliott fit with blue dashed line.

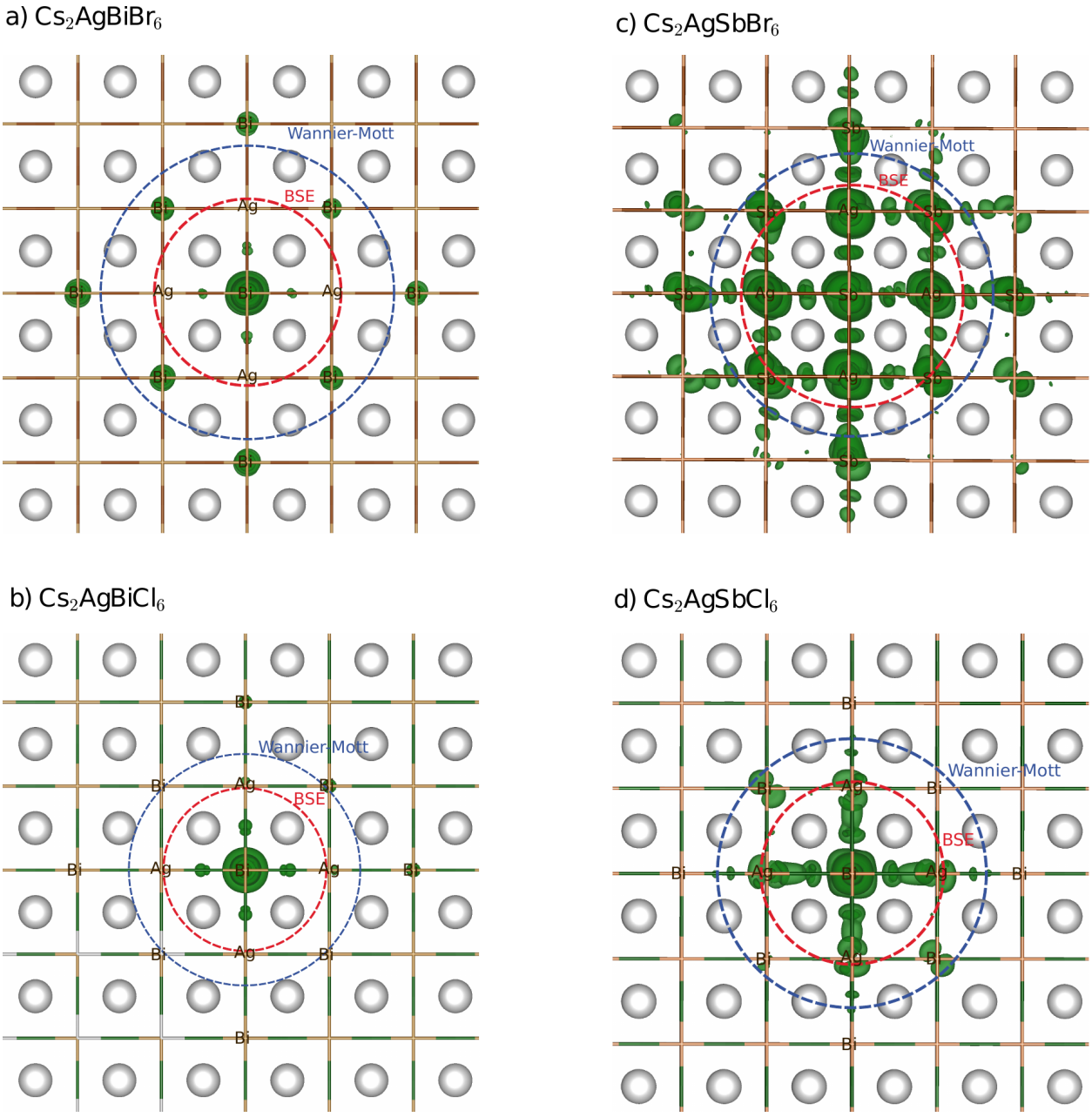

Figure S7: 3D representation of the probability density of the exciton wave function in real space for a) $Cs_2AgBiBr_6$; b) $Cs_2AgBiCl_6$; c) $Cs_2AgSbBr_6$ and d) $Cs_2AgSbCl_6$. We plot an isosurface containing 95% of the excitonic wave function.

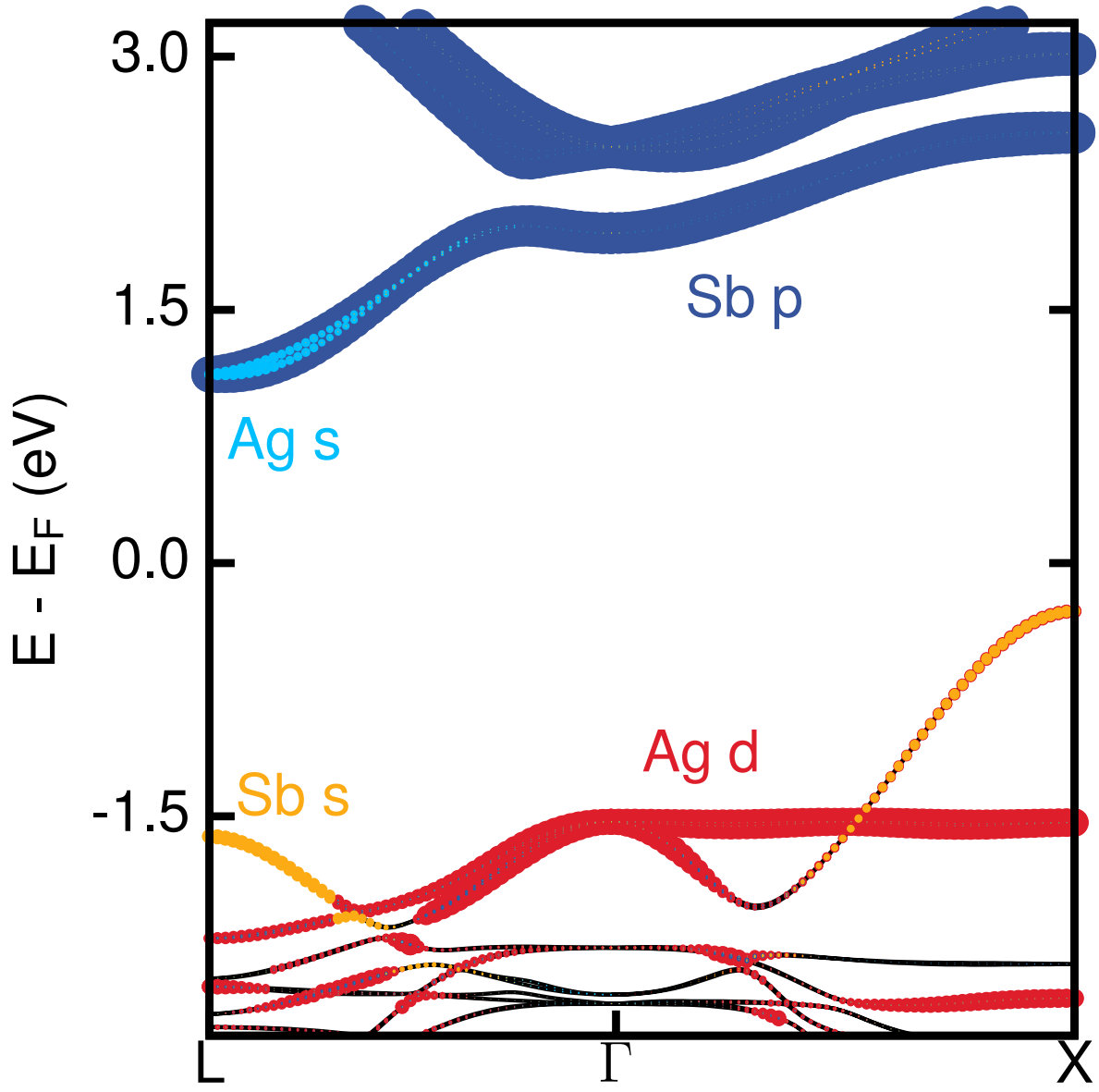

Figure S8: G_0W_0@LDA band structure of $Cs_2AgSbBr_6$. The orbital character of the bands is shown in color (halide character was omitted for clarity).

References

(1) Fetter, A.; Walecka, J. *Quantum Theory of Many-Particle Systems*; MacGraw-Hill: New York, 1971.

(2) Hedin, L. On Correlation Effects in Electron Spectroscopies and the GW Approximation. *J. Phys.: Condens. Matter* **1999**, *11*, R489.

(3) Strinati, G.; Mattausch, H. J.; Hanke, W. Dynamical Correlation Effects on the Quasiparticle Bloch States of a Covalent Crystal. *Phys. Rev. Lett.* **1980**, *45*, 290–294.

(4) Hybertsen, M. S.; Louie, S. G. First-principles Theory of Quasiparticles: Calculation of Band Gaps in Semiconductors and Insulators. *Phys. Rev. Lett.* **1985**, *55*, 1418–1421.

(5) Aryasetiawan, F.; Gunnarson, O. The GW Method. *Rep. Prog. Phys.* **1998**, *61*, 237.

(6) Tamblyn, I.; Darancet, P.; Quek, S. Y.; Bonev, S. A.; Neaton, J. B. Electronic Energy Level Alignment at Metal-Molecule Interfaces with a GW Approach. *Phys. Rev. B* **2011**, *84*, 201402.

(7) van Setten, M. J.; Caruso, F.; Sharifzadeh, S.; Ren, X.; Scheffler, M.; Liu, F.; Lischner, J.; Lin, L.; Deslippe, J. R.; Louie, S. G. et al. GW 100: Benchmarking G_0W_0 for Molecular Systems. *J. Chem. Theory Comput.* **2015**, *11*, 5665–5687.

(8) Hedin, L. New Method for Calculating the One-Particle Green's Function with Application to the Electron-Gas Problem. *Phys. Rev.* **1965**, *139*, A796.

(9) Rohlfing, M.; Louie, S. G. Electron-Hole Excitations and Optical Spectra from First Principles. *Phys. Rev. B* **2000**, *62*, 4927.

(10) Onida, G.; Reining, L.; Rubio, A. Electronic Excitations: Density-Functional versus Many-Body Green's-Function Approaches. *Rev. Mod. Phys.* **2002**, *74*, 601.

(11) Kronik, L.; Neaton, J. B. Excited-State Properties of Molecular Solids from First Principles. *Ann. Rev. Phys. Chem.* **2016**, *67*, 587–616.

(12) Sharifzadeh, S.; Darancet, P.; Kronik, L.; Neaton, J. B. Low-Energy Charge-Transfer Excitons in Organic Solids from First-Principles: The Case of Pentacene. *J. Phys. Chem. Lett.* **2013**, *4*, 2197.

(13) Perdew, J. P.; Zunger, A. Self-interaction Correction to Density-Functional Approximations for Many-Electron Systems. *Phys. Rev. B* **1981**, *23*, 5048–5079.

(14) Ceperley, D. M.; Alder, B. J. Ground State of the Electron Gas by a Stochastic Method. *Phys. Rev. Lett.* **1980**, *45*, 566–569.

(15) Giannozzi, P.; Andreussi, O.; Brumme, T.; Bunau, O.; Nardelli, M. B.; Calandra, M.; Car, R.; Cavazzoni, C.; Ceresoli, D.; Cococcioni, M. et al. Advanced Capabilities for Materials Modelling with QUANTUM ESPRESSO. *J. Phys.: Condens. Matter* **2017**, *29*, 465901.

(16) Giannozzi, P.; Baroni, S.; Bonini, N.; Calandra, M.; Car, R.; Cavazzoni, C.; Ceresoli, D.; Chiarotti, G. L.; Cococcioni, M.; Dabo, I. et al. QUANTUM ESPRESSO: A Modular and Open-Source Software Project for Quantum Simulations of Materials. *J. Phys.: Condens. Matter* **2009**, *21*, 395502 (19pp).

(17) Troullier, N.; Martins, J. L. Efficient Pseudopotentials for Plane-Wave Calculations. *Phys. Rev. B* **1991**, *43*, 1993–2006.

(18) Filip, M. R.; Hillman, S.; Haghighirad, A.-A.; Snaith, H. J.; Giustino, F. Band Gaps of the Lead-Free Halide Double Perovskites $Cs_2BiAgCl_6$ and $Cs_2BiAgBr_6$ from Theory and Experiment. *J. Phys. Chem. Lett.* **2016**, *7*, 2579–2585.

(19) Deslippe, J.; Samsonidze, G.; Strubbe, D. A.; Jain, M.; Cohen, M. L.; Louie, S. G. BerkeleyGW: A Massively Parallel Computer Package for the Calculation of the Quasi-

particle and Optical Properties of Materials and Nanostructures. *Comput. Phys. Commun.* **2012**, *183*, 1269.

(20) Godby, R. W.; Needs, R. J. Metal-Insulator Transition in Kohn-Sham Theory and Quasiparticle Theory. *Phys. Rev. Lett.* **1989**, *62*, 1169.

(21) Pizzi, G.; Vitale, V.; Arita, R.; Blügel, S.; Freimuth, F.; Géranton, G.; Gibertini, M.; Gresch, D.; Johnson, C.; Koretsune, T. et al. Wannier90 as a Community Code: New Features and Applications. *J. Phys.: Condens. Matter* **2020**, *32*, 165902.

(22) Schindlmayr, A. Excitons with Anisotropic Effective Mass. *Euro. J. Phys.* **1997**, *18*, 374–376.

(23) Palummo, M.; Berrios, E.; Varsano, D.; Giorgi, G. Optical Properties of Lead-Free Double Perovskites by Ab Initio Excited-State Methods. *ACS Energy Lett.* **2020**, *5*, 457–463.

(24) Perdew, J. P.; Burke, K.; Ernzerhof, M. Generalized Gradient Approximation Made Simple. *Phys. Rev. Lett.* **1996**, *77*, 3865–3868.